Inorganic Chemistry

pubs.acs.org/IC Article

Synthesis and Cu(I)/Mo(VI) Reactivity of a Bifunctional Heterodinucleating Ligand on a Xanthene Platform

Umesh I. Kaluarachchige Don, Sudheer S. Kurup, Thilini S. Hollingsworth, Cassandra L. Ward, Richard L. Lord,* and Stanislav Groysman*

Cite This: *Inorg. Chem.* 2021, 60, 14655−14666 Read Online

ACCESS | Metrics & More | Article Recommendations | Supporting Information

ABSTRACT: In an effort to probe the feasibility of a model of Mo-Cu CODH (CODH = carbon monoxide dehydrogenase) lacking a bridging sulfido group, the new heterodinucleating ligand LH_2 was designed and its Cu(I)/Mo(VI) reactivity was investigated. LH_2 ((*E*)-3-(((5-(bis(pyridin-2-ylmethyl)amino)-2,7-di-*tert*-butyl-9,9-dimethyl-9*H*-xanthen-4-yl)imino)-methyl)benzene-1,2-diol) features two different chelating positions bridged by a xanthene linker: bis(pyridyl)amine for Cu(I) and catecholate for Mo(VI). LH_2 was synthesized via the initial protection of one of the amine positions, followed by two consecutive alkylations of the second position, deprotection, and condensation to attach the catechol functionality. LH_2 was found to exhibit dynamic cooperativity between two reactive sites mediated by H-bonding of the catechol protons. In the free ligand, catechol protons exhibit H-bonding with imine (intramolecular) and with pyridine (intermolecular in the solid state). The reaction of LH_2 with $[Cu(NCMe)_4]^+$ led to the tetradentate coordination of Cu(I) via all nitrogen donors of the ligand, including the imine. Cu(I) complexes were characterized by multinuclear NMR spectroscopy, high-resolution mass spectrometry (HRMS), X-ray crystallography, and DFT calculations. Cu(I) coordination to the imine disrupted H-bonding and caused rotation away from the catechol arm. The reaction of the Cu(I) complex $[Cu(LH_2)]^+$ with a variety of monodentate ligands X (PPh_3, Cl^-, SCN^-, CN^-) released the metal from coordination to the imine, thereby restoring imine H-bonding with the catechol proton. The second catechol proton engages in H-bonding with Cu−X (X = Cl, CN, SCN), which can be intermolecular (XRD) or intramolecular (DFT). The reaction of LH_2 with molybdate $[MoO_4]^{2-}$ led to incorporation of $[Mo^{VI}O_3]$ at the catecholate position, producing $[MoO_3(L)]^{2-}$. Similarly, the reaction of $[Cu(LH_2)]^+$ with $[MoO_4]^{2-}$ formed the heterodinuclear complex $[CuMoO_3(L)]^-$. Both complexes were characterized by multinuclear NMR, UV−vis, and HRMS. HRMS in both cases confirmed the constitution of the complexes, containing molecular ions with the expected isotopic distribution.

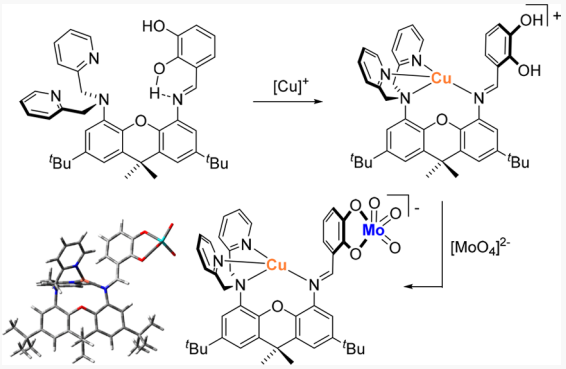

INTRODUCTION

Mo-Cu CO dehydrogenase (CODH) is an air-stable enzyme from the carboxydotrophic bacteria *Oligotropha carboxidovorans* that catalyzes oxidation of CO to CO_2 according to the following equation: $CO + H_2O \rightarrow CO_2 + 2e^- + 2H^+$.[1] The active site and postulated reaction mechanism are presented in Scheme 1. The resting state (**I**) features the Mo(VI) fragment and the Cu(I) fragment linked through a single sulfido bridge.[2,3] The molybdenum center is coordinated by a dithiolene ligand (part of a pyranopterindithiolene cofactor), two oxo/hydroxo groups, and one sulfido group. The copper(I) site is low-coordinate, bearing a cysteinate ligand, a bridging sulfido group, and likely a weakly coordinating water molecule. The unusual composition of this active site and its implication in catalysis has prompted significant interest from the inorganic community. The structural motifs that appear to have an effect on the reactivity are (i) coordination of Mo(VI) by a redox-active dithiolene ligand that stabilizes the formally Mo(VI) oxidation state, (ii) several ligands multiply bonded to Mo(VI), which increases the nucleophilic character of the reactive oxo by decreasing the metal−oxo bond order,[4,5] (iii) coordinative unsaturation at the Cu(I) site, consistent with substrate (CO) coordination,[6,7] and (iv) the proximity of Mo(VI) and Cu(I), enabled by the sulfido bridge. The mechanism of CO oxidation was probed by spectroscopic and computational studies.[8−14] One of the leading current mechanistic hypotheses, supported by DFT calculations, suggests that the initial binding of CO to Cu(I) (**I**-CO) is followed by a nucleophilic attack of Mo-oxo on the

Received: June 9, 2021
Published: September 14, 2021

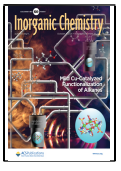

Scheme 1. Active Site (I) and Possible Reaction Mechanism of Mo-Cu CODH

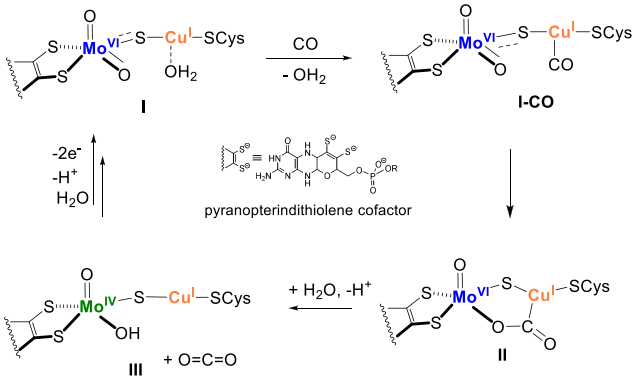

electrophilic carbon of CO to form intermediate **II**. The subsequent oxidation of carbon and reduction of Mo (formally oxo transfer) results in the formation of intermediate **III**, which is reoxidized to **I**. This hypothesis assigns primarily a structural (or structural/electronic) role to the bridging sulfide ligand. We note, however, that other mechanistic hypotheses exist, which propose that the bridging sulfido group also plays a functional role in the oxidation of CO via the formation of a direct chemical bond with the CO carbon and formation of thiocarbonate intermediates.[1]

The validation of structure−function hypotheses described above requires the prior design of appropriate structural models. Significant efforts have been dedicated to modeling the Mo-Cu active site in order to establish its structure−activity relationship.[15] Most of the models specifically pursuing a "Mo−S−Cu" structural motif are displayed in Figure 1. Note

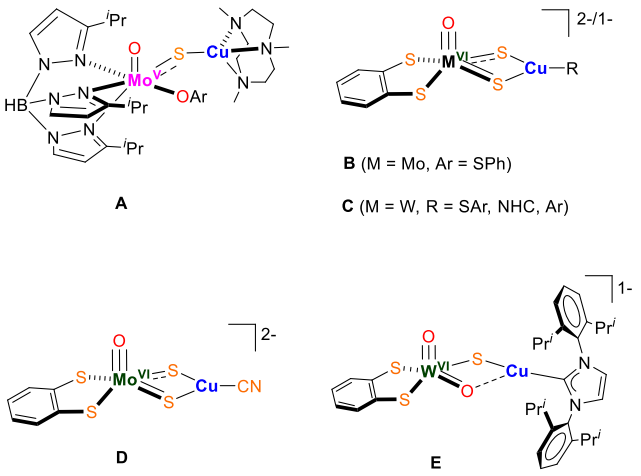

Figure 1. Examples of Mo-Cu CODH models.

that the "$Mo(=O)_2-S-Cu$" motif appears to be inherently unstable for complexes featuring coordinatively unsaturated metals. Young and co-workers reported the $[(Tp)Mo^{V}O(OAr)(\mu_2\text{-}S)Cu^{II}(Me_3tacn)]$ complex **A** (Tp = tris(pyrazolyl)-borate, Me_3tacn = trimethyl-1,4,7-triazacyclononane) bridged by a single sulfido group.[16,17] Tatsumi and co-workers reported the $[(bdt)Mo^{VI}O(\mu_2\text{-}S)_2Cu^{I}(SPh)]$ complex **B** (bdt = benzenedithiolate and related ligands) in which the Mo(VI) center was linked to Cu(I) via two sulfido bridges.[18] As part of their broader investigation on synthetic analogues of molybdoenzymes,[19,20] Holm and co-workers described the synthesis of $[(bdt)W^{VI}O(\mu_2\text{-}S)_2Cu^{I}R]$ (**C**, ;R = thiolate, N-heterocyclic carbene, aryl) and related compounds.[21] The synthetic strategy toward **C** employed the reaction of a previously reported analogue of the XOR active site, $[(bdt)W^{VI}O_2S](NEt_4)_2$,[22,23] with low-coordinate Cu(I) complexes.[24,25] Fontecave and Mougel reported that the closely related $[(bdt)Mo^{VI}O(\mu_2\text{-}S)_2Cu^{I}(CN)]$ complex **D** served as a precatalyst for CO_2 electroreduction.[26] The closest structural model **E**, reported recently by Mankad and co-workers and comprised of the W-based structural model of the Mo-Cu CODH active site, features a single bridging sulfido group that is supported by an additional oxo bridge.[27] We note that structural models usually do not demonstrate the ability of the Cu(I) site to coordinate exogenous substrates (such as CO or related ligands) due to their coordinative saturation and/or surrounding steric bulk necessary for their stabilization.

Our laboratory has explored a different approach to the model of Mo-Cu CODH, where the heterobimetallic site was assembled with the aid of a heterobinucleating xanthene-bridged ligand (Scheme 2).[28] The ligand contains catecholate

Scheme 2. *In Situ* Reactivity of the Mo(VI)-Cu(I) Complex F, in Which the Metals Are Brought Together by a Xanthene-Based Heterodinucleating Ligand

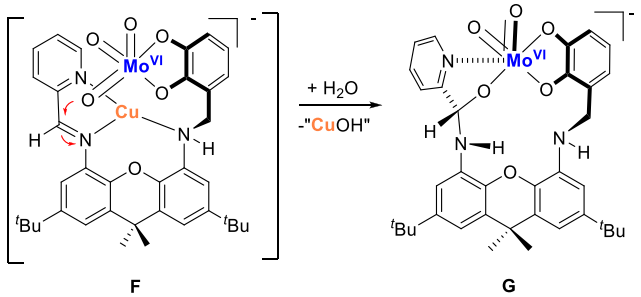

as a dianionic redox-active chelate donor for the $[Mo^{VI}O_3]$ fragment and iminopyridine as a soft donor for Cu(I). This model did not pursue the bridging sulfido group, allowing us to probe its structural vs functional role in a [Mo−S−Cu] unit. The coordination of both metals in **F** triggered oxidation reactivity in which a nucleophilic basal Mo(VI)-oxo functionality attacked a nearby electrophilic Cu(I)-coordinated iminopyridine to produce **G** (Scheme 2). This reactivity provided a possible explanation for the roles of the respective metals even in the absence of the bridging sulfido group. However, due to the hydroxylation of the imine, the heterodinuclear complex proved unstable to isolation, precluding further investigation. Herein we report our initial studies on a new heterodinucleating ligand in which the fragile iminopyridine position was replaced by bis(2-pyridylmethyl)-amine. We show that the Cu(I) site demonstrates variable coordination by the ligand which enables coordination of an exogenous substrate. Most significantly, we demonstrate that the new heterodinucleating ligand enables formation of a relatively stable heterodinuclear Mo(VI)/Cu(I) complex, which forms quantitatively and is characterized in solution by ^{1}H NMR spectroscopy, high-resolution mass spectrometry, (HRMS), and UV−vis spectroscopy. This is the first Mo-Cu CODH model where the metals are positioned in close proximity, and the overall assembly is independent of the

https://doi.org/10.1021/acs.inorgchem.1c01735
Inorg. Chem. 2021, 60, 14655−14666

presence of the bridging sulfido(s) group. As was mentioned, such a model can help to probe the precise role of the sulfido group in the reaction mechanism. Furthermore, a model containing adjacent Mo(VI) and Cu(I) but lacking a bridging sulfido group allows a test of the feasibility of alternative Mo-Cu CODH mechanistic intermediates in which the metals are not bridged by a sulfido group, such as thiocarbonate.[1,2,12]

EXPERIMENTAL SECTION

(*E*)-3-(((5-(Bis(pyridin-2-ylmethyl)amino)-2,7-di-*tert*-butyl-9,9-dimethyl-9*H*-xanthen-4-yl)imino)methyl)benzene-1,2-diol (LH_2). 2,7-Di-*tert*-butyl-9,9-dimethyl-*N*,*N*-bis(pyridin-2-ylmethyl)-xanthene-4,5-diamine (**III**; 1.00 g, 1.8 mmol) was added to a stirred 150 mL solution of 2,3-dihydroxybenzaldehyde (0.310 g, 2.2 mmol) in ethanol. The reaction mixture was stirred for 24 h. The solvent was removed *in vacuo*, and the product was purified by recrystallization from a minimal amount of benzene. The product LH_2 was obtained in 81% yield (0.896 g). ^{1}H NMR (600 MHz, CD_2Cl_2): δ 14.46 (br s, 1H, catechol-OH), 8.90 (s, 1H, imine-H), 8.43 (d, $^3J_{HH}$ = 4.6 Hz, 2H, α -H on pyridine), 7.42 (d, $^4J_{HH}$ = 2 Hz, 1H, *o*-H on pyridinyl xanthene side), 7.36 (m, 3H, γ-H on pyridine, 4-H on catechol), 7.24 (d, $^3J_{HH}$ = 7.9 Hz, 2H, β'-H on pyridine), 7.19 (d, $^4J_{HH}$ = 2.3 Hz, 1H, *p*-H on pyridinyl xanthene side), 7.07 (d, $^4J_{HH}$ = 2 Hz, 1H, *p*-H on catechol xanthene side), 7.02 (m, 3H, 6-H on catechol, β-H on pyridine), 6.82 (t, $^3J_{HH}$ = 7.7 Hz, 2H, 5-H on catechol), 6.78 (d, $^4J_{HH}$ = 2 Hz, 1H, *o*-H on catechol xanthene side), 6.35 (br s, 1H, catechol-OH), 4.55 (s, 4H, methylene-H), 1.68 (s, 6H, methyl-H), 1.40 (s, 9H, *tert*-butyl-H on catechol xanthene side), 1.17 (s, 9H, *tert*-butyl-H on pyridinyl xanthene side) ppm. ^{13}C{^{1}H} NMR (CD_2Cl_2, 150 MHz): δ 163.52, 159.67, 151.39, 149.10, 146.48, 146.08, 145.71, 142.98, 142.13, 137.97, 136.15, 135.31, 131.78, 130.33, 128.71, 123.35, 123.16, 122.01, 121.58, 120.52, 119.01, 118.90, 117.60, 116.68, 115.87, 58.86, 35.39, 35.08, 34.80, 32.18, 31.66, 31.46 ppm. HRMS (ESI$^+$): *m*/*z* 655.3645 (calculated *m*/*z* 655.3648 for $[LH_2 + H]^+$). Mp: 168−170 °C.

Preparation of $[Cu(LH_2)](PF_6)$ ($1(PF_6)$). A 3 mL solution of tetrakis(acetonitrile)copper(I) hexafluorophosphate $[Cu(NCMe)_4](PF_6)$ (8.5 mg, 0.023 mmol, 1.0 equiv) in acetonitrile and a 3 mL solution of LH_2 (15 mg, 0.023 mmol, 1.0 equiv) in acetonitrile were prepared and cooled to −33 °C. The solution of cold LH_2 was then added dropwise to a stirred solution of cold $[Cu(NCMe)_4](PF_6)$, producing a red-brown solution. The reaction mixture was stirred for 1 h, upon which the volatiles were removed *in vacuo*. The product was obtained as a red-brown solid. This solid was purified by recrystallization from CH_2Cl_2/diethyl ether, which yielded red-brown crystals of $\mathbf{1}(PF_6)$ (18.7 mg, 0.022 mmol, 95%). ^{1}H NMR (CD_3CN, 600 MHz): δ 8.82 (s, ^{1}H, imine-H), 8.55 (d, $^3J_{HH}$ = 4.9 Hz, 2H, α-H on pyridine), 7.62 (t, $^3J_{HH}$ = 7.7 Hz, 2H, γ-H on pyridine), 7.51 (d, $^4J_{HH}$ = 1.9 Hz, 1H, *o*-H on pyridinyl xanthene side), 7.44 (d, $^4J_{HH}$ = 1.6 Hz, 1H, *p*-H on pyridinyl xanthene side), 7.38 (t, $^4J_{HH}$ = 1.9 Hz, 1H, *p*-H on catechol xanthene side), 7.29 (t, $^3J_{HH}$ = 6.4 Hz, 2H, β-H on pyridine), 7.24 (d, $^4J_{HH}$ = 1.6 Hz, 1H, *o*-H on catechol xanthene side), 7.14 (d, $^3J_{HH}$ = 7.7 Hz, 1H, 4-H on catechol), 7.03 (d, $^3J_{HH}$ = 7.7 Hz, 2H, β'-H on pyridine), 6.93 (d, $^3J_{HH}$ = 7.8 Hz, 1H, 6-H on catechol), 6.88 (t, $^3J_{HH}$ = 7.8 Hz, 1H, 5-H on catechol), 4.54 (s, 4H, methylene-H), 1.70 (s, 6H, methyl-H), 1.39 (s, 9H, *tert*-butyl-H on catechol xanthene side), 1.18 (s, 9H, *tert*-butyl-H on pyridinyl xanthene side) ppm. ^{13}C{^{1}H} NMR (CD_3CN, 150 MHz): δ 166.34, 158.05, 150.45, 149.64, 147.83, 146.50, 146.4, 145.22, 141.05, 139.14, 137.54, 135.34, 131.63, 130.77, 125.25, 124.92, 124.87, 124.20, 122.70, 120.05, 119.98, 119.24, 116.95, 68.26, 59.11, 35.58, 35.53, 35.26, 33.38, 31.60, 31.44, 26.22 ppm. HRMS (ESI$^+$): *m*/*z* 716.2782 (calculated *m*/*z* for $[Cu(LH)^+$ 716.2788). λ_{max}, nm (ε_M, L mol^{-1} cm^{-1}): 348 (sh, 8600), 268 (23000), 253 (22000). Anal. Calcd for $C_{42}H_{46}CuF_6N_4O_3P{\cdot}2H_2O$: C, 56.09; H, 5.60; N, 6.23. Found: C, 55.99; H, 5.25; N, 6.34.

Preparation of $[Cu(LH_2)](PF_6)$ ($1(PF_6)$) from $[Cu(LH_2)(Cl)]$ (4). A 3 mL solution of **4** (20 mg, 0.026 mmol, 1.0 equiv) in CH_3CN and a 3 mL solution of thallium hexafluorophosphate (9.3 mg, 0.026 mmol, 1.0 equiv) in CH_3CN were prepared and cooled to −33 °C. The solution of cold thallium hexafluorophosphate was then added dropwise to a stirred solution of cold **4**, producing a red-brown solution. The reaction mixture was stirred for 1 h, upon which the solution was filtered. The filtrate was removed *in vacuo*. The product ($\mathbf{1}(PF_6)$) was obtained as a red-brown solid, and its nature was confirmed by ^{1}H NMR spectroscopy (22.1 mg, 0.024 mmol, 91%).

Preparation of $[Cu(LH_2)(PPh_3)](PF_6)$ ($2(PF_6)$). A 3 mL solution of triphenylphosphine (7.6 mg, 0.029 mmol, 1.0 equiv) in CH_3CN was added dropwise to a stirred 5 mL solution of complex **1** (PF_6) (25 mg, 0.029 mmol, 1.0 equiv) in CH_3CN. The reaction mixture was stirred for 1 h, upon which the volatiles were removed *in vacuo*. This solid was purified by recrystallization from CH_2Cl_2/diethyl ether, which yielded orange-yellow crystals of $[Cu(LH_2)(PPh_3)](PF_6)$ ($\mathbf{2}(PF_6)$; 31.2 mg, 0.028 mmol, 95%). ^{1}H NMR (CD_2Cl_2, 600 MHz): δ 14.07 (br s, 1H, catechol-OH), 8.75 (s, 1H, imine-H), 8.13 (d, $^3J_{HH}$ = 3.6 Hz, 2H, α-H on pyridine), 7.57 (t, $^3J_{HH}$ = 7.2 Hz, 2H, γ-H on pyridine), 7.53 (s, 1H, *o*-H on pyridinyl xanthene side), 7.48 (m, 2H, *p*-H on pyridinyl xanthene side, *p*-H on catechol xanthene side), 7.38 (m, 15H, H on triphenylphosphine), 7.18 (m, 3H, β-H on pyridine, *o*-H on catechol xanthene side), 7.14 (d, $^3J_{HH}$ = 7.2 Hz, 1H, 4-H on catechol), 6.97 (d, $^3J_{HH}$ = 7.2 Hz, 3H, β'-H on pyridine, 6-H on catechol), 6.90 (t, $^3J_{HH}$ = 6.8 Hz, 1H, 5-H on catechol), 5.10 (br s, 1H, catechol-OH), 4.80 (m, 4H, methylene-H), 1.67 (s, 6H, methyl-H), 1.42 (s, 9H, *tert*-butyl-H on catechol xanthene side), 0.78 (s, 9H, *tert*-butyl-H on pyridinyl xanthene side) ppm. ^{13}C{^{1}H} NMR (CD_2Cl_2, 150 MHz): δ 164.68, 157.50, 149.70, 147.85, 146.74, 145.44, 145.37, 138.82, 134.92, 133.96, 133.86, 132.50, 132.27, 132.15, 131.15, 130.92, 129.62, 129.61, 129.54, 125.66, 124.43, 124.38, 123.66, 123.17, 122.14, 119.85, 118.39, 117.26, 115.82, 60.08, 35.26, 35.23, 34.64, 32.70, 31.60, 31.20, ppm. HRMS (ESI$^+$): *m*/*z* 979.3772 (calculated *m*/*z* for $[Cu(LH_2)(PPh_3)]^+$ 979.3799).

Preparation of $[Cu(LH_2)(SCN)]$ (3). A 6 mL solution of copper(I) thiocyanate (6.8 mg, 0.076 mmol, 2.0 equiv) in CH_3CN and a 3 mL solution of LH_2 (25 mg, 0.038 mmol, 1.0 equiv) in CH_3CN were prepared and cooled to −33 °C. The solution of cold LH_2 was then added dropwise to a stirred solution of cold copper(I) thiocyanate, producing a pale brown solution. The reaction mixture was stirred for 1 h, upon which the volatiles were removed *in vacuo*. The product $[Cu(LH_2)(SCN)]$ (**3**) was obtained as a red-brown solid (28.1 mg, 0.036 mmol, 95%). ^{1}H NMR (CD_2Cl_2, 600 MHz): δ 14.35 (br s, 1H, catechol-OH), 8.78 (s, 1H, imine-H), 8.72 (d, $^3J_{HH}$ = 3.9 Hz, 2H, α-H on pyridine), 7.89 (s, 1H, *o*-H on pyridinyl xanthene side) 7.53 (t, $^3J_{HH}$ = 7.2 Hz, 2H, γ-H on pyridine), 7.47 (s, 1H, *o*-H on catechol xanthene side), 7.30 (s, 1H, *p*-H on pyridinyl xanthene side), 7.28 (t, $^3J_{HH}$ = 6.1 Hz, 2H, β-H on pyridine), 7.19 (s, 1H, *p*-H on catechol xanthene side), 7.13 (d, $^3J_{HH}$ = 7.2 Hz, 1H, 4-H on catechol), 6.99 (d, $^3J_{HH}$ = 7.6 Hz, 1H, 6-H on catechol), 6.90 (t, $^3J_{HH}$ = 7.8 Hz, 1H, 5-H on catechol), 6.83 (d, $^3J_{HH}$ = 7.6 Hz, 2H, β'-H on pyridine), 5.32 (br s, 1H, catechol-OH), 4.50(s, 4H, methylene-H), 1.70 (s, 6H, methyl-H), 1.42 (s, 9H, *tert*-butyl-H on catechol xanthene side), 1.20 (s, 9H, *tert*-butyl-H on pyridinyl xanthene side) ppm. ^{13}C{^{1}H} NMR (CD_2Cl_2, 150 MHz): δ 164.27, 157.37, 150.65, 149.77, 147.22, 146.93, 146.11, 145.71, 141.11, 137.46, 135.97, 135.04, 131.12, 130.81, 127.98, 124.15, 124.05, 123.50, 122.14, 122.00, 119.57, 118.79, 118.01, 115.39, 59.23, 35.18, 34.93, 32.80, 31.63, 31.45 ppm. HRMS (ESI$^+$): *m*/*z* 388.6381 (calculated *m*/*z* for $\{[Cu(LH_2)(SCN)] + 2H\}^{2+}$ 388.6387).

Preparation of $[Cu(LH_2)(Cl)]$ (4). A 3 mL solution of copper(I) chloride (6.1 mg, 0.061 mmol, 1.0 equiv) in CH_3CN and a 3 mL solution of LH_2 (40 mg, 0.061 mmol, 1.0 equiv) in CH_3CN were prepared and cooled to −33 °C. The solution of cold LH_2 was then added dropwise to a stirred solution of cold copper(I) chloride, producing a pale brown solution. The reaction mixture was stirred for 1 h, upon which the volatiles were removed *in vacuo*. The product was obtained as a brown solid. This solid was purified by recrystallization from CH_2Cl_2/CH_3CN, which yielded red-brown crystals of $[Cu(LH_2)(Cl)]$ (**4**; 44.3 mg, 0.059 mmol, 96%). ^{1}H NMR (CD_2Cl_2, 600 MHz): δ 14.32 (br s, 1H, catechol-OH), 8.79 (s, 1H, imine-H), 8.75 (s, 2H, α-H on pyridine), 7.91 (s, 1H, *o*-H on pyridinyl xanthene

https://doi.org/10.1021/acs.inorgchem.1c01735
Inorg. Chem. 2021, 60, 14655−14666

side), 7.48 (t, $^3J_{HH}$ = 7.6 Hz, 2H, γ-H on pyridine), 7.46 (d, $^4J_{HH}$ = 1.3 Hz, 1H, *o*-H on catechol xanthene side), 7.24 (s, 1H, *p*-H on pyridinyl xanthene side), 7.22 (t, $^3J_{HH}$ = 6.4 Hz, 2H, β-H on pyridine), 7.19 (d, $^4J_{HH}$ = 1.3 Hz, 1H, *p*-H on catechol xanthene side), 7.12 (d, $^3J_{HH}$ = 7.9 Hz, 1H, 4-H on catechol), 7.01 (d, $^3J_{HH}$ = 7.6 Hz, 1H, 6-H on catechol), 6.88 (t, $^3J_{HH}$ = 7.7 Hz, 1H, 5-H on catechol), 6.84 (d, $^3J_{HH}$ = 7.2 Hz, 2H, β′-H on pyridine), 5.64 (br s, 1H, catechol-OH), 4.48 (s, 4H, methylene-H), 1.69 (s, 6H, methyl-H), 1.41 (s, 9H, *tert*-butyl-H on catechol xanthene side), 1.16 (s, 9H, *tert*-butyl-H on pyridinyl xanthene side) ppm. $^{13}C\{^1H\}$ NMR (CD_2Cl_2, 150 MHz): δ 164.16, 157.57, 150.79, 149.86, 147.01, 146.78, 146.02, 145.86, 141.35, 139.78, 136.99, 135.97, 135.61, 131.30, 130.40, 124.12, 123.69, 123.37, 122.02, 120.96, 119.44, 118.90, 118.04, 115.38, 59.07, 35.20, 35.16, 35.08, 32.67, 31.65, 31.45 ppm. HRMS (ESI^+): *m*/*z* 376.6311 (calculated *m*/*z* for $\{[Cu(LH_2)(Cl)]+H\}^{2+}$ 376.6317). Anal. Calcd for $C_{42}H_{46}ClCuN_4O_3{\cdot}0.5CH_2Cl_2$: C, 64.10; H, 5.95; N, 7.04. Found: C, 64.34; H, 5.55; N, 7.09.

Preparation of $[Cu_2(LH_2)(CN)_2]$ (5). A 6 mL solution of copper(I) cyanide (6.8 mg, 0.076 mmol, 2.0 equiv) in CH_3CN and a 3 mL solution of LH_2 (25 mg, 0.038 mmol, 1.0 equiv) in CH_3CN were prepared and cooled to −33 °C. The solution of cold LH_2 was then added dropwise to a stirred solution of cold copper(I) cyanide, producing a pale brown solution. The reaction mixture was stirred for 1 h, upon which the volatiles were removed *in vacuo*. The product was obtained as a red-brown solid. This solid was purified by recrystallization from CH_2Cl_2/hexane, which yielded red-brown crystals of $[Cu_2(LH_2)(CN)_2]$ (**5**; 30.2 mg, 0.036 mmol, 95%). ^1H NMR (CD_2Cl_2, 600 MHz): δ 14.25 (br s, 1H, catechol-OH), 8.77 (s, 1H, imine-H), 8.70 (br s, 2H, α-H on pyridine), 7.94 (s, 1H, *o*-H on pyridinyl xanthene side), 7.52 (t, $^3J_{HH}$ = 6.8 Hz, 2H, γ-H on pyridine), 7.48 (s, 1H, *o*-H on catechol xanthene side), 7.34 (s, 1H, *p*-H on pyridinyl xanthene side), 7.28 (br t, 2H, β-H on pyridine), 7.18 (s, 1H, *p*-H on catechol xanthene side), 7.13 (d, $^3J_{HH}$ = 6.9 Hz, 1H, 4-H on catechol), 7.00 (d, $^3J_{HH}$ = 7.2 Hz, 1H, 6-H on catechol), 6.89 (t, $^3J_{HH}$ = 7.2 Hz, 1H, 5-H on catechol), 6.83 (d, $^3J_{HH}$ = 6.9 Hz, 2H, β′-H on pyridine), 5.48 (br s,1H, catechol−OH), 4.54 (s, 4H, methylene-H), 1.71 (s, 6H, methyl-H), 1.41 (s, 9H, *tert*-butyl-H on catechol xanthene side), 1.21 (s, 9H, *tert*-butyl-H on pyridinyl xanthene side) ppm. $^{13}C\{^1H\}$ NMR (CD_2Cl_2, 150 MHz): δ 164.42, 157.55, 150.53, 149.70, 147.31, 146.83, 145.76, 145.73, 141.04, 137.75, 136.12, 135.25, 131.06, 130.96, 128.13, 123.98, 123.93, 123.46, 122.23, 122.14, 119.62, 118.86, 118.19, 115.49, 59.59, 35.26, 35.19, 32.87, 31.64, 31.58 ppm. HRMS (ESI^+): *m*/*z* 744.2969 (calculated *m*/*z* for $[Cu(LH_2)(CN)]^+$ 744.2975).

Preparation of $(Et_4N)_2[MoO_3(L)]$ ($(Et_4N)_2$6). A 3 mL solution of tetraethylammonium molybdate $(NEt_4)_2[MoO_4]$ (12.8 mg, 0.031 mmol, 1.0 equiv) in CH_3CN and a 3 mL solution of LH_2 (20 mg, 0.031 mmol, 1.0 equiv) in CH_3CN were prepared and cooled to −33 °C. The solution of cold LH_2 was then added dropwise to a stirred solution of cold $(NEt_4)_2[MoO_4]$. The reaction mixture was stirred for 30 min, after which the volatiles were removed *in vacuo* to produce a dark yellow solid of $(Et_4N)_2[MoO_3(L)]$ ($(Et_4N)_2$**6**; 26.5 mg, 0.029 mmol, 94%). ^1H NMR (CD_2Cl_2, 600 MHz): δ 9.09 (s, 1H, imine-H), 8.41 (d, $^3J_{HH}$ = 4.3 Hz, 2H, α -H on pyridine), 7.40 (d, $^3J_{HH}$ = 3.6 Hz, 4H, γ-H on pyridine, β′-H on pyridine), 7.31 (d, $^3J_{HH}$ = 7.6 Hz, 1H, 4-H on catechol), 7.23 (d, $^4J_{HH}$ = 1 Hz, 1H, *o*-H on pyridinyl xanthene side), 7.02 (m, 3H, *p*-H on catechol xanthene side, β-H on pyridine), 6.97 (d, $^4J_{HH}$ = 1 Hz, 1H, *p*-H on pyridinyl xanthene side), 6.75 (d, $^4J_{HH}$ = 0.7 Hz, 1H, *o*-H on catechol xanthene side), 6.49 (d, $^3J_{HH}$ = 7.2 Hz, 1H, 6-H on catechol), 6.23 (t, $^3J_{HH}$ = 7.6 Hz, 1H, 5-H on catechol), 4.62 (s, 4H, methylene-H), 3.17 (q, $^3J_{HH}$ = 7.1 Hz, 16H, methylene-H on tetraethylammonium), 1.64 (s, 6H, methyl-H), 1.37 (s, 9H, *tert*-butyl-H on catechol xanthene side), 1.15 (m, 33H, *tert*-butyl-H on pyridinyl xanthene side, methyl-H on tetraethylammonium) ppm. ^1H NMR (CD_3CN, 600 MHz): δ 8.98 (s, 1H, imine-H), 8.39 (d, $^3J_{HH}$ = 4.6 Hz, 2H, α-H on pyridine), 7.46 (t, $^3J_{HH}$ = 7.8 Hz, 2H, β-H on pyridine), 7.43 (d, $^3J_{HH}$ = 7.8 Hz, 2H, β′-H on pyridine), 7.28 (d, $^4J_{HH}$ = 2 Hz, 1H, *o*-H on pyridinyl xanthene side), 7.17 (d, $^3J_{HH}$ = 7.9 Hz, 1H, 4-H on catechol), 7.05 (m, 3H, *p*-H on catechol xanthene side, γ-H on pyridine), 6.98 (d, $^4J_{HH}$ = 2 Hz, 1H, *p*-H on pyridinyl xanthene side), 6.86 (d, $^4J_{HH}$ = 1.6 Hz, 1H, *o*-H on catechol xanthene side), 6.36 (d, $^3J_{HH}$ = 6.2 Hz, 1H, 6-H on catechol), 6.5 (t, $^3J_{HH}$ = 7.6 Hz, 1H, 5-H on catechol), 4.67 (s, 4H, methylene-H), 3.17 (q, $^3J_{HH}$ = 7.2 Hz, 16H, methylene-H on tetraethylammonium), 1.61 (s, 6H, methyl-H), 1.38 (s, 9H, *tert*-butyl-H on catechol xanthene side), 1.16 (m, 33H, *tert*-butyl-H on pyridinyl xanthene side, methyl-H on tetraethylammonium) ppm. $^{13}C\{^1H\}$ NMR (CD_2Cl_2, 150 MHz): δ 160.80, 160.00, 159.38, 149.00, 146.04, 145.03, 143.33, 142.73, 142.39, 138.06, 136.65, 130.80, 130.71, 123.49, 121.95, 120.12, 119.06, 118.19, 115.96, 115.08, 114.27, 113.63, 113.02, 58.69, 54.24, 52.81, 52.79, 52.77, 35.37, 35.02, 34.77, 31.88, 31.84, 31.51, 7.81 ppm. IR (cm^{-1}): 895 (s), 848 (vs), 825 (vs). HRMS (ESI^-): *m*/*z* 799.2346 (calculated *m*/*z* for $[7 + H]^-$ 799.2393). λ_{max}, nm (ε_M, L mol^{-1} cm^{-1}): 406 (9300), 294 (14000), 252 (26000).

Preparation of $(Et_4N)[CuMoO_3(L)]$ ((Et_4N)7). A 3 mL solution of $[Cu(LH_2)](PF_6)$ (**1**(PF_6); 20 mg, 0.023 mmol, 1.0 equiv) in CH_3CN and a 3 mL solution of tetraethylammonium molybdate $(NEt_4)_2[MoO_4]$ (9.7 mg, 0.023 mmol, 1.0 equiv) in CH_3CN were prepared and cooled to −33 °C. The solution of cold **1**(PF_6) was then added dropwise to a stirred solution of chilled $(NEt_4)_2[MoO_4]$, producing a red-brown solution. Monitoring the reaction by ^1H NMR and HRMS demonstrated the clean formation of (Et_4N)7. ^1H NMR (CD_3CN, 400 MHz): δ 8.63 (s, 1H, imine-H), 8.15 (d, $^3J_{HH}$ = 4.7 Hz, 2H, β′-H on pyridine), 7.53, 7.50 (m, 4H, γ-H on pyridine, α-H on pyridine), 7.28 (d, $^4J_{HH}$ = 2 Hz, 1H, *o*-H on pyridinyl xanthene side), 7.21 (d, $^4J_{HH}$ = 2 Hz, H, *p*-H on pyridinyl xanthene side,), 7.17 (d, $^4J_{HH}$ = 1.6 Hz, 1H, *p*-H on catechol xanthene side), 7.06 (d, $^4J_{HH}$ = 2 Hz, 1H, *o*-H on catechol xanthene side),7.02 (m, 3H, β-H on pyridine, 6-H on catechol) 6.68 (d, $^3J_{HH}$ = 7 Hz, 1H, 4-H on catechol), 6.44 (t, $^3J_{HH}$ = 7.6 Hz, 1H, 5-H on catechol), 5.12 (br s, 4H, methylene-H), 3.16 (q, $^3J_{HH}$ = 7.4 Hz, 8H, methylene-H on tetraethylammonium), 1.52 (s, 6H, methyl-H), 1.36 (s, 9H, *tert*-butyl-H on catechol xanthene side), 1.20 (m, 21H, *tert*-butyl-H on pyridinyl xanthene side, methyl-H on tetraethylammonium) ppm. HRMS (ESI^+) *m*/*z* 862.1748 (calculated *m*/*z* for $[7 + H]^-$862.1689). λ_{max}, nm (ε_M, L mol^{-1} cm^{-1}): 424 (5300), 330 (9600), 292 (15000), 242 (27000). (Et_4N)7 decomposes in solution to produce an orange precipitate, which was investigated by HRMS and XPS. HRMS (ESI^+): *m*/*z* 1560.4371 (calculated *m*/*z* for $[MoO_2Cu_2L_2]^+$ 1560.4433), 862.1714 (calculated for $[7 + H]^-$ 862.1689), 780.2214 (calculated for $[MoO_2Cu_2L_2]^{2+}$ 780.2186), 716.2803 (calculated *m*/*z* for $[Cu(LH)]^+$ 716.2788).

Preparation of $(Et_4N)[CuMoO_3(L)]$ ((Et_4N)7) from $[Cu(LH_2)(Cl)]$ (4). A 3 mL solution of **4** (20 mg, 0.026 mmol, 1.0 equiv) in CD_3CN and a 3 mL solution of tetraethylammonium molybdate $(NEt_4)_2[MoO_4]$ (11.16 mg, 0.026 mmol, 1.0 equiv) in CD_3CN were prepared and cooled to −33 °C. The solution of cold **4** was then added dropwise to a stirred solution of chilled $(NEt_4)_2[MoO_4]$, producing a red-brown solution. The nature of the product ((Et_4N)7) was confirmed by ^1H NMR spectroscopy.

RESULTS AND DISCUSSION

Ligand Synthesis. The abbreviated synthesis of LH_2 (LH_2 = (*E*)-3-(((5-(bis(pyridin-2-ylmethyl)amino)-2,7-di-*tert*-butyl-9,9-dimethyl-9*H*-xanthen-4-yl)imino)methyl)benzene-1,2-diol) is presented in Figure 2. Xanthene diamine (2,7-di-*tert*-butyl-9,9-dimethyl-4,5-xanthene diamine) has been extensively used as a linker for various homodinucleating and, less commonly, heterodinucleating ligands.[29−42] Hess and co-workers reported the synthesis of a heterodinucleating xanthene-based ligand featuring bis(2-pyridylmethyl)amine and iminopyridine sites, via the intermediacy of compounds **I** and **II** (obtained as a mixture and separated by column chromatography).[43] Similar to the strategy reported by Hess and co-workers, our synthetic strategy toward LH_2 involved initial *tert*-butoxycarbonyl (Boc) protection of one of the amine positions, followed by alkylation of the second position

https://doi.org/10.1021/acs.inorgchem.1c01735
Inorg. Chem. 2021, 60, 14655−14666

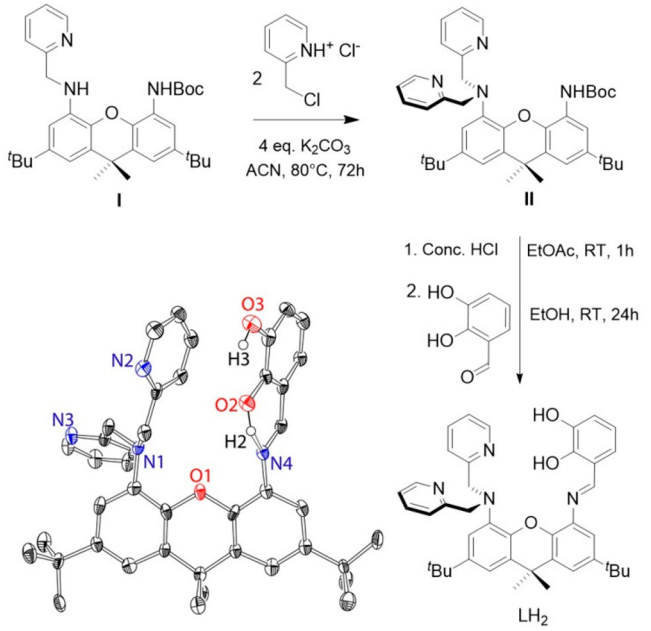

Figure 2. Synthesis and structure of LH_2 with 50% probability ellipsoids. Hydrogen atoms (except for the catechol hydrogens) and the cocrystallized benzene molecule are omitted for clarity.

to give the previously reported compound **I**. Carrying out the second alkylation step for a significantly longer period of time (72 h) and using a different solvent mixture (CH_3CN/H_2O) allowed us to obtain compound **II** in 62% yield. Following the synthesis of **II**, it was deprotected and condensed with 2,3-dihydroxybenzaldehyde to give the final product LH_2 in 28% overall yield. A detailed synthetic scheme is provided in Scheme S1 in the Supporting Information.

LH_2 was characterized by ^1H and ^{13}C NMR spectroscopy, high-resolution mass spectrometry (HRMS), and X-ray crystallography. The protons were assigned with the help of 2D $^1H-^1H$ COSY spectroscopy (see the Supporting Information for details). Among other characteristic spectroscopic features, the xanthene *tert*-butyl groups give rise to two different peaks (1.40 and 1.17 ppm in CD_2Cl_2), consistent with the nonsymmetric substitution pattern of LH_2. In contrast, a single set of resonances is obtained for the xanthene methyl groups and 2-methylpyridyl groups, consistent with an effective C_s symmetry of the ligand. Notably, catechol protons give rise to two NMR signals featuring drastically different chemical shifts: 14.46 and 6.35 ppm. The downfield chemical shift (14.46 ppm) suggests strong intramolecular hydrogen bonding.[44,45] The lack of a ^{13}C resonance around 180 ppm indicates that the compound is not in the enaminoketone form.[46] The X-ray structure of the ligand (Figure 2) confirms the overall connectivity and reveals intramolecular H-bonding between O2*H2* and a nearby imine (N4). In contrast, intermolecular H-bonding is observed between O3*H3* and the pyridine of the neighboring ligand. Both hydrogens were identified from the difference map and isotropically refined.

Synthesis and Reactions of Cu(I) Complexes. Following the synthesis of the ligand, its reactivity with Cu(I) was explored (Scheme 3). The reaction of LH_2 with $[Cu(NCMe)_4](PF_6)$ produced the copper(I) complex $[Cu(LH_2)](PF_6)$ ($\mathbf{1}(PF_6)$), isolated as red-brown crystals in 95% yield. $\mathbf{1}(PF_6)$ was characterized by ^1H and ^{13}C NMR spectroscopy, UV–vis spectroscopy, HRMS, and X-ray crystallography.

Scheme 3. Synthesis and Reactions of the Cu(I) Complex with LH_2

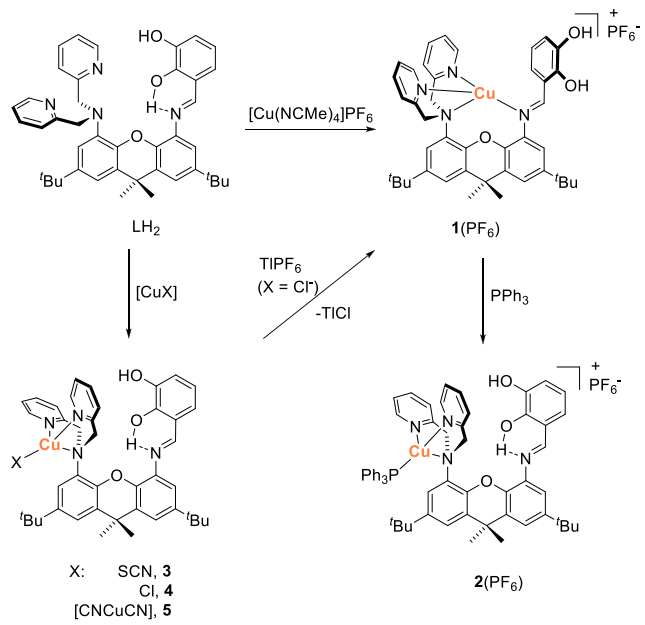

HRMS demonstrates the presence of $[Cu(LH_2) - H]^+$ ion in the positive mode (see the Supporting Information); the peak attributed to $[Cu(LH_2) - H]^+$ is consistent with the expected isotopic distribution. The ^1H NMR spectrum suggests metal coordination via the bis(2-pyridylmethyl)amine site: while the catechol aryl protons chemical shifts are largely unaffected by Cu(I) coordination, there is a significant shift in the resonances of the pyridine protons. Notably, despite the expected coordination of both 2-pyridylmethyl arms to Cu(I), the methylene protons of $[CH_2C_5H_5N]$ appear as a singlet, as in the spectrum of the free ligand. Catechol O*H* protons were not observed in the ^1H NMR spectrum.

The X-ray structure of $\mathbf{1}(PF_6)$, obtained from CH_2Cl_2/ether (Figure 3, left), confirms copper(I) incorporation at the designated site and provides a rationale for the spectroscopic observations. The structure demonstrates metal coordination by all four nitrogens of the ligand, including the imine nitrogen (N4). Both pyridines and the imine bind relatively strongly (bond distances of 2.06(1), 2.01(1), and 2.02(1) Å, respectively). In contrast, only a borderline interaction between Cu(I) and the central amine (N1) is observed (2.43(1) Å). The distance between Cu(I) and the xanthene oxygen is 2.63(1) Å, which is significantly larger than the sum of the ionic radii.[47] We postulate that the Cu(I) coordination to the imine weakens the coordination of the amine nitrogen. The resulting dynamic behavior equilibrates the AB protons of the methylene arms, resulting in their appearance as a singlet in the ^1H NMR spectrum. The catechol site does not participate in metal coordination. Furthermore, as the imine nitrogen is not available for hydrogen bonding, the catechol rotates away from the metal and engages in hydrogen bonding with two ether molecules. A different polymorph of **1** (PF_6) ($\mathbf{1}'(PF_6)$; Figure 3, right), obtained from THF/ether, demonstrates very similar structural features: Cu–N2 and Cu–N3 (pyridine) bonds of 2.022(5) and 2.033(4) Å, a Cu–N4 (imine) bond of 2.031(4) Å, and a long Cu–N1 (amine) distance of 2.432(4) Å. The major difference between the structures is that in

https://doi.org/10.1021/acs.inorgchem.1c01735
Inorg. Chem. 2021, 60, 14655–14666

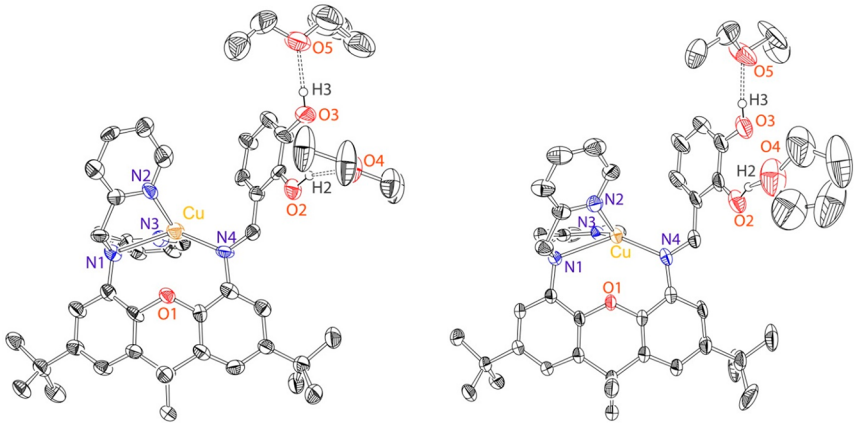

Figure 3. (left) The structure of **1**(PF_6) with 50% probability ellipsoids. (right) The structure of **1′**(PF_6) with 50% probability ellipsoids. PF_6 counterions, hydrogen atoms (except for the catechol hydrogens), and cocrystallized solvent (except for the H-bonded ether/THF molecules) are omitted for clarity.

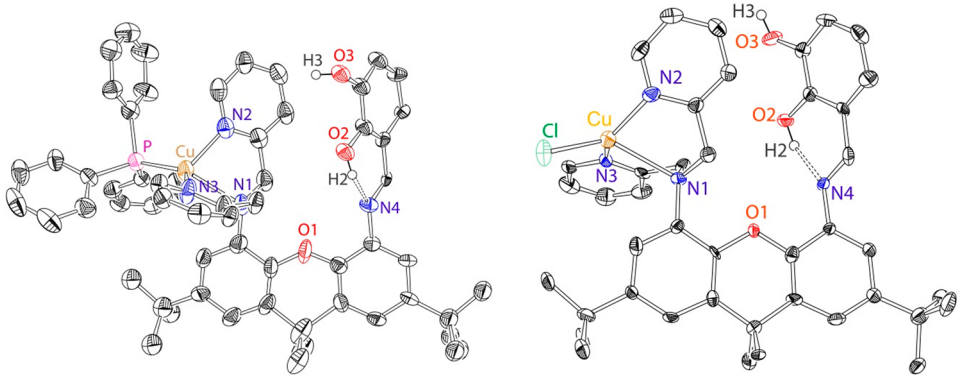

Figure 4. (left) X-ray structure of **2**(PF_6) with 50% probability ellipsoids. The alternate conformation of parts of **2**(PF_6), H atoms (other than catechol OH hydrogens), PF_6 counterions, and cocrystallized solvent were omitted for clarity. (right) Structure of **4** with 50% probability ellipsoids. Only one of the two independent molecules present in the asymmetric unit is shown. H atoms (other than catechol OH hydrogens), the PF_6 counterion, and cocrystallized solvent molecules are omitted for clarity.

1′(PF_6) one of the ethers is replaced by THF as an H-bond acceptor.

DFT calculations were performed at the BP86/def2SVP level of theory with no ligand simplifications (see the Supporting Information for full computational details). Optimization of $\mathbf{1}^+$ without the counterion produced a structure with $Cu-N_{imine}$ = 2.057 Å, $Cu-N_{pyridine}$ = 2.043/2.067 Å, and $Cu-N_{amine}$ = 2.488 Å. These compare well with the crystallographically determined distances. Unsurprisingly, an analysis of the frontier orbitals does not show any significant covalent Cu−L bonding interactions, given the d^{10} configuration of the Cu(I) ion. Rotation about the $C_{imine}-C_{catechol}$ bond allows us to explore what effect a hydrogen bond to the imine nitrogen would have on this structure ($\mathbf{1a}^+$). While such a species is a well-defined minimum, the formation of that hydrogen bond is not enough to disrupt the $Cu-N_{imine}$ interaction, though it does elongate to 2.143 Å. The hydrogen bond is relatively weak with a long H···N distance of 1.877 Å (*vide infra*) and is due to the nonplanarity (dihedral angle 18°) of the pseudo-six-membered ring involving that hydrogen bond. Collectively, this causes $\mathbf{1a}^+$ to be 2.85 kcal/mol higher in free energy than $\mathbf{1}^+$, consistent with experimental observations even in the absence of coordinating solvent molecules interacting with the catechol hydroxyl groups.

Tetradentate coordination of Cu(I) by LH_2 creates a potential obstacle for the coordination of small molecules (including CO) to the copper site. To probe the ability of the copper site to coordinate exogenous ligands, we have explored the formation of triphenylphosphine, thiocyanate, chloride, and cyanide complexes (Scheme 3). The complexes [Cu(LH_2)(PPh_3)](PF_6) (**2**(PF_6)), [Cu(LH_2)(SCN)] (**3**), and [Cu(LH_2)(Cl)] (**4**) were synthesized by the addition of the respective monodentate ligand to **1**(PF_6) or by the reaction of LH_2 with the respective precursor CuX. In the case of the cyanide ligand, the reaction of the $[CuCN]_n$ precursor with LH_2 led to isolation of the dicopper dicyanide complex ([Cu_2(LH_2)($CN)_2$], **5**). This reaction outcome is ascribed to an excess of CuCN used in the reaction and to the well-known ability of cyanide to serve as a bridging ligand.

We have also attempted the reaction of **1**(PF_6) with CO. Replacing the atmosphere of solution **1**(PF_6) by an atmosphere of CO resulted in a color change to blood red, and the initial NMR spectra collected under CO suggested the formation of a new compound (Figure S33). However, this NMR decays quickly to the familiar NMR spectrum of **1**(PF_6) in the absence of CO. Furthermore, the IR spectrum of the sample lacking the CO atmosphere indicated the lack of a CO band. The crystallization attempt produced the crystals of **1′**(PF_6). Thus, it is feasible that CO coordination initially takes

https://doi.org/10.1021/acs.inorgchem.1c01735
Inorg. Chem. 2021, 60, 14655−14666

place, similar to the coordination of PPh_3. We hypothesize that, since CO is a weaker donor for Cu(I), the product quickly converts back to **1**(PF_6).

All complexes were obtained as red-orange crystalline solids and were characterized by ^1H and ^{13}C NMR spectroscopy, HRMS, and X-ray crystallography (except for **3**). All complexes exhibited the molecular peak ($[Cu(LH_2)(X)]^+$) in HRMS, consistent with coordination of the exogenous ligand. The ^{31}P NMR spectrum of **2**(PF_6) contains a signal at 2.66 ppm (CD_3CN, vs −5.90 ppm for free PPh_3) consistent with PPh_3 coordination to the metal. Several notable features were observed in the proton NMR spectra of **2**−**5**. Similar to **1**, the methylene protons of **3**−**5** appear as a singlet, suggesting a weak bond to the central amine. The methylene protons of **2**, however, appear as a broad doublet. In sharp contrast to **1**(PF_6), all complexes exhibit characteristic catechol proton signals at around 5−6 and 14−15 ppm. The latter downfield signal suggests strong intramolecular hydrogen bonding between the catechol O*H* and imine, similar to the catechol H-bonding pattern observed for LH_2. As such a pattern would require free imine, it is likely that coordination of the exogenous ligand breaks the Cu(I)−imine bond.

X-ray crystallography carried out on **2**(PF_6) (Figure 4, left), **4** (Figure 4, right), and **5** (Figure 5) confirmed their structures

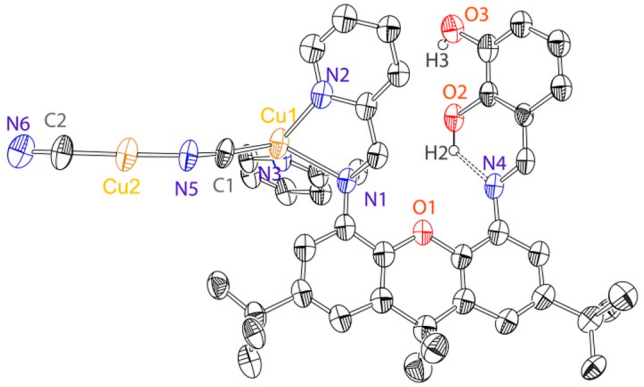

Figure 5. X-ray structure of **5** with 50% probability ellipsoids. H atoms (except for catechol OH hydrogens) and cocrystallized solvent molecules are omitted for clarity.

and corroborated the spectroscopic findings. All structures demonstrate coordination of an exogenous ligand to the metal that triggers the metal release from imine ligation and ensuing rotation of the bis(pyridine)amine site away from the xanthene linker. In contrast, the catechol rotates back and forms an intramolecular H-bond with the imine (N4). We were able to identify the positions of the H-bonded catechol hydrogen (H2; see Figures 4 and 5) from the difference map in the structures of complexes **2**(PF_6), **4**, and **5**. The observed H-bonding pattern between the catechol OH and the imine is further supported by the *syn*-coplanar arrangement of the imine and the catechol in both structures and drastically different chemical shifts of catechol OH protons (**2**(PF_6), 14.07 and 5.10 ppm; **5**, 14.25 and 5.48 ppm).

2(PF_6) and **4** exhibit mononuclear structures featuring tetracoordinate copper(I) centers. Two slightly different conformers of $[Cu(LH_2)(Cl)]$ occupy the asymmetric unit of **4**. While the overall structural features of the two different conformers of **4** are similar, their copper sites exhibit somewhat different metrics, consistent with the structural lability of copper(I). As an example, the distances between the metal and central amine are 2.374(6) and 2.468(6) Å, suggesting borderline coordination in both conformers. The bond distance between the metal and the central amine in **2**(PF_6) is shorter (2.281(7) Å). Stronger bonding between the metal and the amine is consistent with the lack of equilibration of the $NCH_2C_5H_5N$ (methylene) protons in the spectrum of **2**(PF_6). Copper-bound chloride serves as an intermolecular H-bond acceptor in the structure of **4** (with the second catechol proton, H3), resulting in the formation of chains.

Complex **5** contains two distinct copper sites (Figure 5). Similar to the structures of other $[Cu(LH_2)X]$ complexes, the Cu1 site is tetracoordinate and exhibits stronger coordination by the pyridines (2.04(1) and 2.02(1) Å), weaker bonding with the central amine (2.33(1) Å), and coordination to the carbon of the proximal cyanide ligand (1.86(2) Å). The same cyanide is bridging to the second, two-coordinate copper site Cu2 through N5 (1.83(1) Å). The coordination environment of Cu2 is accomplished by C-coordination of the distal cyanide. The nitrogen end of the distal cyanide serves as an intermolecular catechol H-bond acceptor.

The spectroscopic and structural findings presented above paint a clear picture of the dynamic behavior of the bifunctional ligand LH_2. Two reactive sites of LH_2 exhibit cooperative behavior mediated by intramolecular hydrogen bonding of the catechol and the imine. In the free ligand, strong intramolecular H-bonding is observed between one of the catechol protons and the imine, enforcing the *syn*-coplanar conformation of the catechol. Copper(I) coordination by LH_2 engages the imine donor, releasing it from the hydrogen bonding and enabling the catechol to rotate away and participate in hydrogen bonding with external acceptors. Coordination of an exogenous ligand to copper(I) decoordinates the imine. As a result, the copper site swings away from the imino/xanthene linker, while catechol rotates back and establishes the observed intramolecular H-bonding with the imine. For one specific ligand (chloride), this behavior is reversible: removal of the chloride (using $TlPF_6$) from $[Cu(LH_2)(Cl)]$ (**4**) restores the complex $[Cu(LH_2)(PF_6)]$ (**1**(PF_6)) (Scheme 3). Notably, the second catechol proton participates in the interaction with the exogenous (Lewis basic) ligand at the copper site (Cl^- and CN^-; see Figure S47). While the crystallographically observed interaction is intermolecular, one cannot preclude an intramolecular H-bonding for the complex in solution. To probe this and other questions concerning the solution structure of this species, we conducted DFT calculations.

The DFT optimization of **4** involved a number of structural variables in the starting structure: (i) rotation about the $C_{xanthene}-N_{amine}$ bond, (ii) rotation about the $C_{imine}-C_{catechol}$ bond, (iii) conformational flexibility in the methylpyridine arms, and (iv) *syn*/*anti* forms of the catechol hydroxyl groups. Shown in Figure 6 are the four lowest free energy optimized structures: **4a** (0.00 kcal/mol), **4b** (0.68 kcal/mol), **4c** (4.66 kcal/mol), and **4d** (7.84 kcal/mol). **4b** is most similar to the crystallographically observed structure, but the lack of an intermolecular Cl···HO hydrogen bond likely makes it less favorable than **4a** in our computational model. Both of these isomers and **4d** demonstrate strong intramolecular bonding to the imine with OH···N distances of 1.582, 1.577, and 1.585 Å for **4a**, **4b**, and **4d**, respectively. **4a** and **4d** display intramolecular Cl···HO hydrogen bonding between catechol and chloride. Simulated spectral features (IR and ^1H NMR)

https://doi.org/10.1021/acs.inorgchem.1c01735
Inorg. Chem. 2021, 60, 14655−14666

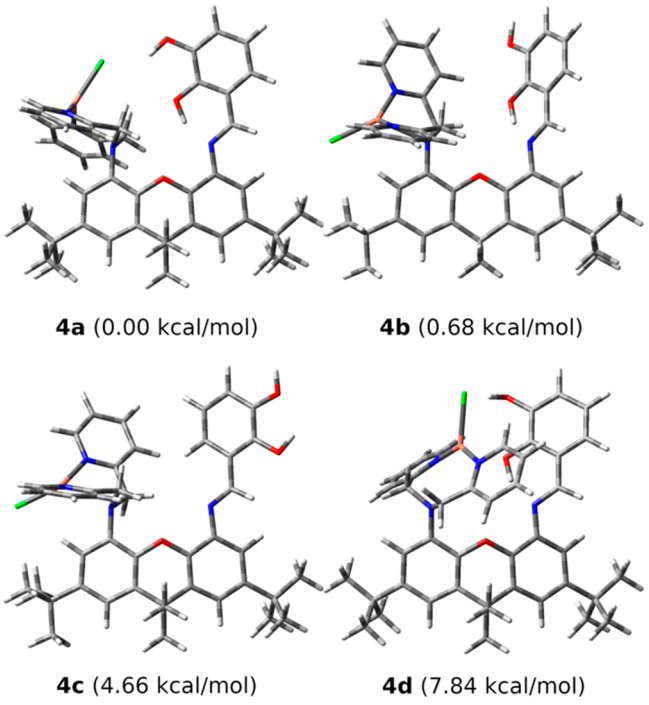

Figure 6. Optimized structures of **4a** (top left), **4b** (top right), **4c** (bottom left), and **4d** (bottom right). Relative free energies are given in kcal mol^{-1}.

did not provide a clear fingerprint that would allow us to distinguish **4a** and **4b**, but simulated ^{1}H chemical shifts reinforce the assignment of the catechol protons and rule out significant concentrations of any isomer with catechol rotated such that the intramolecular imine hydrogen bond cannot form (see Table S2).

Synthesis and Characterization of Mo(VI) and Heterodinuclear Cu(I)/Mo(VI) complexes. Following the structural, spectroscopic, and computational investigation of $[Cu(LH_2)]$ complexes, we turned to studying the incorporation of molybdenum(VI) (Scheme 4). Treatment of a cold

Scheme 4. Synthesis of $(Et_4N)_2$6

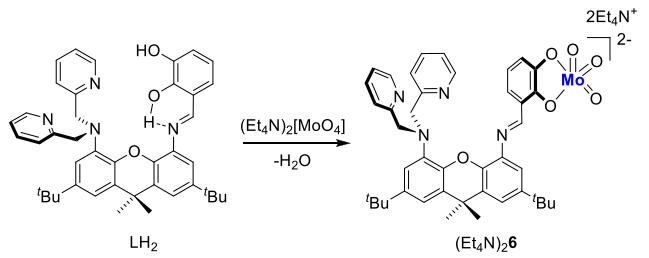

(−33 °C) acetonitrile solution of $(Et_4N)_2[MoO_4]$ with an acetonitrile solution of LH_2 led to the formation of $(Et_4N)_2[MoO_3(L)]$ ($(Et_4N)_2$**6**), isolated as a dark yellow solid. $(Et_4N)_2$**6** was characterized by ^{1}H and ^{13}C NMR spectroscopy, UV−vis spectroscopy, IR spectroscopy, and HRMS. Our multiple attempts to crystallize $(Et_4N)_2$**6** failed to produce X-ray-quality crystals, generally leading to the formation of a yellow microcrystalline material. However, the nature of $(Et_4N)_2$**6** was unequivocally established by ^{1}H and ^{13}C NMR spectroscopy and especially HRMS. HRMS (ESI^+) demonstrates the presence of the molecular peak at m/z 799.2346, consistent with $[MoO_3(L) + H]^+$ (Figure 7). The isotopic distribution of the signal correlates with the expected

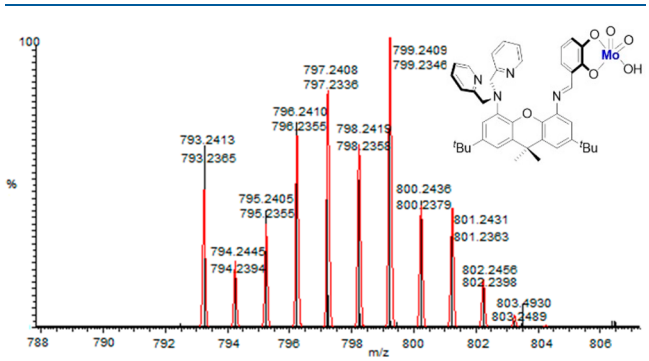

Figure 7. HRMS (ESI^+) of $(Et_4N)_2$**6**. The black lines represent the observed spectrum and the red lines the calculated spectrum for $[MoO_2(OH)L]^+$.

distribution for $[MoO_3(L) + H]^+$. ^{1}H NMR (CD_2Cl_2) contains no catechol O*H* protons, consistent with its deprotonation. Moreover, an upfield shift is observed for the aryl (catecholate) protons in comparison with the free ligand or with copper(I) complexes, again suggesting deprotonation and molybdate incorporation. In contrast, the pyridine protons resonate at chemical shifts close to those of the free ligand, suggesting the lack of metal coordination at this site. We also note that $(Et_4N)_2$**6** appears to be indefinitely stable in solution at RT: no visible change in the ^{1}H NMR spectrum was observed after 6 days (see Figure S28). This is in contrast to the fate of the previously reported $(Et_4N)_2[MoO_3(L')]$ (where L′ was the iminopyridine-based heterodinucleating ligand; see Scheme 2), which underwent disproportionation in solution to $(Et_4N)_2[MoO_2(L')_2]$ and $(Et_4N)_2[MoO_4]$.[28] It is hypothesized that $(Et_4N)_2$**6** is more stable due to the overall bulkier nature of the ligand and possible weak stabilizing interaction of the pyridines with the Mo(VI) center.

Dropwise addition of a cold acetonitrile solution of **1**(PF_6) to $(Et_4N)_2[MoO_4]$ produced a red-brown solution. Monitoring the reaction by ^{1}H NMR spectroscopy demonstrated the clean formation of a new species consistent with the heterodinuclear $(Et_4N)[CuMoO_3(L)]$ complex (Et_4N)**7** (Scheme 5). In addition, the formation of H_2O and $(Et_4N)(PF_6)$ was also observed; the formation of $(Et_4N)(PF_6)$ was further confirmed by X-ray crystallography (unit cell determination). The reaction of $[Cu(LH_2)(Cl)]$ (**4**) with $(Et_4N)_2[MoO_4]$ leads to the formation of the same heterobimetallic product (Et_4N)**7**, along with$(Et_4N)Cl$. ^{1}H NMR of (Et_4N)**7** (Figure S29) demonstrates a shift in the aryl catecholate protons consistent with the incorporation of $[MoO_3]$. Thus, the three aryl catechol protons (CD_3CN) in **1**(PF_6) appear at 7.14, 6.92, and 6.88 ppm, whereas $(Et_4N)_2$**6** gives rise to signals at 7.17, 6.36, and 6.15 ppm. The corresponding protons are observed at 7.02, 6.67, and 6.44 ppm for (Et_4N)**7**. Cu(I) coordination by (Et_4N)**7** (including the imine donor) is suggested by the appearance of $[CH_2C_5H_5N]$ methylene protons as a broad resonance. In contrast, $[CH_2C_5H_5N]$ give rise to a sharp singlet in $(Et_4N)_2$**6**, which does not have bound Cu(I). UV−vis spectroscopy demonstrates the formation of new species with spectral features combining those of $(Et_4N)_2$**6** and **1**(PF_6) (see Figure S51). Thus, $(Et_4N)_2$**6** displayed signals at 406, 294, and 252 nm and **1**(PF_6) demonstrated peaks at 348, 268, and 253 nm.

https://doi.org/10.1021/acs.inorgchem.1c01735
Inorg. Chem. 2021, 60, 14655−14666

Scheme 5. Reactions of Cu(I) Complexes 1(PF_6) and 4 with (Et_4N)$_2$[MoO_4] to Produce the Complex (Et_4N)7

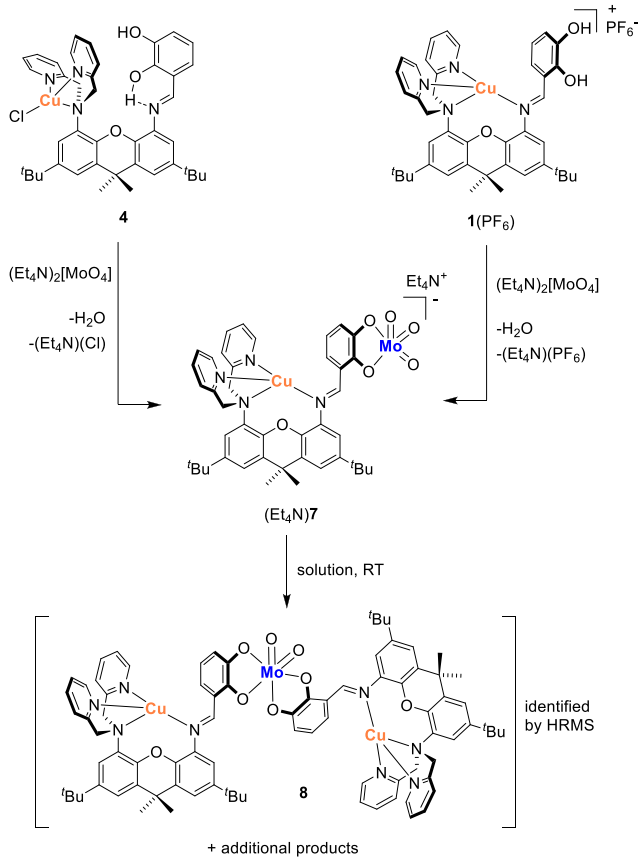

(Et_4N)7 exhibits peaks at 424, 330 (shoulder), 292, and 242 nm. Most significantly, the identity of (Et_4N)7 was established by high-resolution mass spectrometry. The HRMS spectrum contains the expected peak for the heterodinuclear molecular ion at m/z 862.1748, consistent with the [$CuMoO_2$(OH)(L)]$^+$ formulation (Figure 8). Furthermore, the observed isotopic distribution pattern matches well with the expected isotopic distribution of the heterodinuclear Cu(I)-Mo(VI) complex [$CuMoO_2$(OH)(L)]$^+$.

DFT optimization of 7$^-$ produced multiple rotational isomers similar to **4** (see the Supporting Information for full details), but one isomer was much lower (6.54 kcal/mol from next closest isomer) in free energy than the others. The structure of the geometry-optimized structure of 7$^-$ is shown in Figure 9. The Cu(I) ion has short Cu−$N_{pyridine}$ = 2.009/2.051 Å and Cu−N_{imine} = 2.026 Å distances. The Cu−N_{amine} bond is elongated by ∼0.1 Å relative to the optimized structure of **1** at 2.585 Å, suggesting that Cu(I) is three-coordinate in this structure. MoO_3 is bound to catecholate with short and long Mo−O distances of 2.115 and 2.476 Å. Such a large difference in the Mo−$O_{catecholate}$ bond lengths is due to a significant distortion from the idealized square-planar geometry, which results in only one of the oxo groups exerting a *trans* influence at a Mo−catecholate bond. Holm and co-workers have demonstrated that a similar isomer of (Et_4N)$_2$[WO_3(Cl_2bdt)] also exhibited a difference between the W−S_{Cl2bdt} bonds as a result of a *trans* influence, although the difference was significantly smaller (∼0.1 Å).[22] Significantly larger Mo−$O_{catecholate}$ bond length differences of up to 0.25 Å were reported in octahedral [MoO_2(catecholate)$_2$]$^{2-}$, where only one of the two catecholate oxygens was *trans* to oxo.[48−50] The catecholate is rotated away from the Cu center about the C_{imine}−$C_{catecholate}$ bond. All optimized isomers demonstrated similar coordination environments for the Cu(I)/Mo(VI) ions. The simulated UV−vis spectrum of 7$^-$ in acetonitrile shows a peak at 450 nm and is similar to the experimental spectrum (Figure S55). This transition is a catecholate $\pi \rightarrow$ imine π^* transition. This explains why the lowest energy feature of the experimental spectrum for **6** shifts from 406 to 424 nm upon binding of Cu, since the copper ion lowers the imine π^* orbital energy that results in the red shift. Unfortunately, the simulated spectra of the rotational isomers of 7$^-$ are similar; thus, this does not allow us to distinguish the dominant isomer in solution, other than ruling out 7**d**$^-$. The simulated ^{1}H NMR shifts are also in reasonable agreement with experiment (Table S5).

(Et_4N)7 exhibits limited stability in solution that is concentration-dependent. At ∼12 mM, the initially transparent solution demonstrates the formation of an orange precipitate after approximately 30 min. At a lower concentration (∼4 mM), the solution remains transparent at RT (no change in the proton spectrum) for at least 2 h. However, concentration of the solution under vacuum increases the decomposition

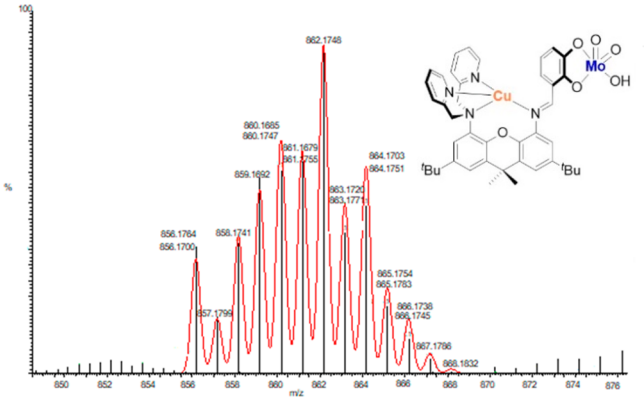

Figure 8. HRMS (ESI) of (Et_4N)7. The black lines represent the observed spectrum and the red lines the calculated spectrum for [$CuMoO_2$(OH)L]$^+$.

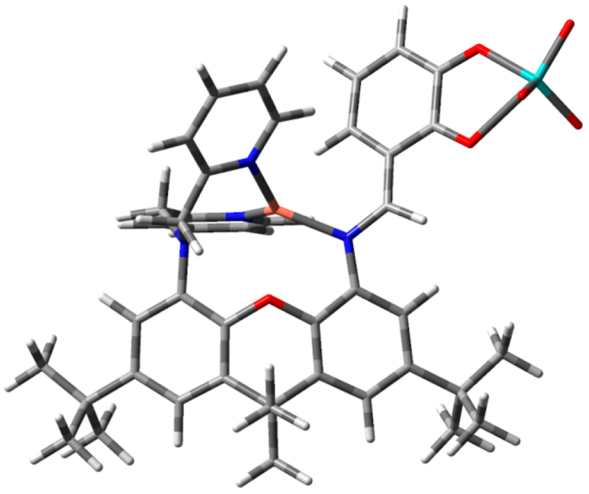

Figure 9. Optimized structure of 7$^-$.

https://doi.org/10.1021/acs.inorgchem.1c01735
Inorg. Chem. 2021, 60, 14655−14666

rate, as formation of the precipitate is observed. We have followed the decomposition of the sample of (Et_4N)**7** by ^{1}H NMR spectroscopy (see Figure S31) for 24 h. The decomposition follows second order kinetics with $k = 2.2 \times 10^{-6}$ M^{-1} s^{-1} (Figure S32). The resulting orange precipitate was characterized by ^{1}H NMR, HRMS, and XPS. The precipitate was not soluble, or only sparingly soluble, in most organic solvents (benzene, THF, dichloromethane, acetonitrile, DMSO, DMF). NMR characterization of the orange precipitate in DMF-d_7, benzene-d_6, or DMSO-d_6 demonstrated poorly resolved spectra. High-resolution mass spectrometry, however, revealed the presence of positive ions attributed to the trimetallic $[MoO_2Cu_2L_2]$ (**8**; Scheme 5), including peaks at m/z 1560.4371 (expected m/z 1560.4433 for $[MoO_2Cu_2L_2]^+$) and 780.2214 (expected m/z of 780.2186 for $[MoO_2Cu_2L_2]^{2+}$) with the isotopic distribution matching singly and doubly charged species, accordingly (Figures S42–S44). The peak at m/z 749.7625 likely corresponds to the doubly charged bimetallic species $[MoO_2CuL_2]^{2+}$. The attempted reactions of (Et_4N)**7** with an additional 1 equiv of LH_2 or **1**(PF_6) (to isolate the corresponding bimetallic and trimetallic complexes $[MoO_2CuL_2]^-$ and $[MoO_2Cu_2L_2]$) produced mixtures of compounds featuring broad NMR spectra. However, their high-resolution mass spectra were generally in line with the expectations, demonstrating the corresponding trimetallic and bimetallic complexes. X-ray photoelectron spectroscopy (see the Supporting Information) revealed the presence of both copper and molybdenum in the precipitate, along with carbon, nitrogen, and oxygen. The amount of copper was significantly higher in comparison with molybdenum. Although Mo(VI) was the predominant oxidation state, Mo(IV) was also detected. We postulate that the reactive molybdenum trioxo mono(catecholate) complex $[MoO_3CuL]^-$ ((Et_4N)**7**) undergoes disproportionation to form the molybdenum dioxo bis(catecholate) complex $[MoO_2Cu_2L_2]$ (**8**), along with molybdate. A similar disproportionation was previously reported for the related monometallic molybdenum trioxo mono(catecholate) species[28] and is likely driven by the nucleophilicity of molybdenum trioxo. Following their initial formation, both **8** and molybdate could undergo additional reactions, including the formation of μ-oxo bridges, which could be responsible for the formation of the insoluble material. In our future work, we will aim to prevent this disproportionation by transforming one of the oxos in $[MoO_3CuL]^-$ into the bulkier and less nucleophilic alkoxo/siloxo functionalities. It is emphasized that, in stark contrast to **F**, which could not be directly observed and was only postulated as part of the reaction mechanism, (Et_4N)**7** forms quantitatively (by ^{1}H NMR), is directly observed, and exhibits at least moderate stability in solution under ambient conditions. This could enable its reactivity studies in the future.

SUMMARY AND CONCLUSIONS

The active site of Mo-Cu carbon monoxide dehydrogenase features a $[Mo^{VI}O_2(\mu_2\text{-}S)Cu^I]$ disposition, in which two nearby metals are bridged with a single sulfido bridge. While the sulfido bridge plays an important structural function, by holding the two metals together, its functional role is less clear. An understanding of the precise functional role of the bridging sulfido may be of importance in the future design of biomimetic heterobimetallic CO/CO_2 interconversion catalysts. To probe the feasibility of the Mo-Cu CODH model lacking a bridging sulfido group, we have previously designed and synthesized a xanthene-bridged heterodinucleating ligand, which combined catecholate and iminopyridine sites. While that ligand enabled separate coordination of Mo(VI) and Cu(I) at the designated positions, the reactive nature of the iminopyridine precluded the isolation of the heterodinuclear species. Our present work described the synthesis of a new heterodinucleating ligand and its stable Cu(I), Mo(VI), *and* directly observable and relatively stable heterodinuclear Cu(I)/Mo(VI) complex. We have demonstrated that the Cu(I) site is capable of coordinating exogenous monodentate ligands, including PPh_3, Cl^-, SCN^-, and CN^-. Furthermore, we have shown that the imine position plays the role of a mediator between the two ligand sites. In the absence of an additional ligand at Cu(I), it serves as a Cu(I) donor. Upon coordination of Cl^- or other ligands to Cu(I), it releases Cu(I) and serves as an H-bond acceptor to one of the catechol protons, enforcing its *syn*-coplanar stereochemistry. We also demonstrated that the second catechol proton forms an H-bond with the Cu–Cl function. It is noted that this particular coordination behavior is specific to the mononuclear (Cu) complexes, as upon Mo coordination, the overall assembly will lack the H bonds. However, it is still feasible that the imine may exhibit coordination/decoordination behavior in the corresponding heterodinuclear complex: for example, upon installation of the exogenous and/or bridging ligand. Given the ability of the present system to (i) coordinate an additional ligand to Cu(I), (ii) form relatively stable Cu(I)/Mo(VI) species, and (iii) demonstrate cooperativity between the metal binding sites, this could enable a study of its reactivity in the future.

ASSOCIATED CONTENT

Supporting Information

The Supporting Information is available free of charge at https://pubs.acs.org/doi/10.1021/acs.inorgchem.1c01735.

General experimental details, synthetic procedures concerning compounds **I**–**III**, crystallographic and computational details, and NMR, UV–vis, and mass spectra (PDF)

xyz structures for all optimized geometries (XYZ)

Accession Codes

CCDC 2073154–2073159 contain the supplementary crystallographic data for this paper. These data can be obtained free of charge via www.ccdc.cam.ac.uk/data_request/cif, or by emailing data_request@ccdc.cam.ac.uk, or by contacting The Cambridge Crystallographic Data Centre, 12 Union Road, Cambridge CB2 1EZ, UK; fax: +44 1223 336033.

AUTHOR INFORMATION

Corresponding Authors

Richard L. Lord − *Department of Chemistry, Grand Valley State University, Allendale, Michigan 49401, United States;* orcid.org/0000-0001-6692-0369; Email: lordri@gvsu.edu

Stanislav Groysman − *Department of Chemistry, Wayne State University, Detroit, Michigan 48202, United States;* orcid.org/0000-0003-3578-7985; Email: groysman@wayne.edu

Authors

Umesh I. Kaluarachchige Don − *Department of Chemistry, Wayne State University, Detroit, Michigan 48202, United States*

Sudheer S. Kurup − *Department of Chemistry, Wayne State University, Detroit, Michigan 48202, United States*

Thilini S. Hollingsworth − *Department of Chemistry, Wayne State University, Detroit, Michigan 48202, United States*

Cassandra L. Ward − *Lumigen Instrument Center, Wayne State University, Detroit, Michigan 48202, United States;* orcid.org/0000-0001-6736-6769

Complete contact information is available at: https://pubs.acs.org/10.1021/acs.inorgchem.1c01735

Notes

The authors declare no competing financial interest.

■ ACKNOWLEDGMENTS

We dedicate this manuscript to the memory of Prof. R. H. Holm, a great mentor, a pioneer in bioinorganic chemistry, and a true connoisseur of inorganic synthesis. S.G. is grateful to the ACS PRF for current support under grant number 58937-ND3. Experimental characterization was carried out at the Lumigen Instrument Center of Wayne State University. We thank Ms. Hashini N. Munasinghe and Dr. S. Sameera Perera for experimental assistance.

■ REFERENCES

(1) Hille, R.; Dingwall, S.; Wilcoxen, J. The Aerobic CO Dehydrogenase from OligotrophaCarboxidovorans. *JBIC, J. Biol. Inorg. Chem.* **2015**, *20*, 243−251.

(2) Dobbek, H.; Gremer, L.; Kiefersauer, L.; Huber, R.; Meyer, O. Catalysis at a Dinuclear [CuSMo(=O)OH] Cluster in a CO Dehydrogenase Resolved at 1.1 Å Resolution. *Proc. Natl. Acad. Sci. U. S. A.* **2002**, *99*, 15971−15976.

(3) Gnida, M.; Ferner, R.; Gremer, L.; Meyer, O.; Meyer-Klaucke, W. A Novel Binuclear [CuSMo] Cluster at the Active Site of Carbon Monoxide Dehydrogenase: Characterization by X-ray Absorption Spectroscopy. *Biochemistry* **2003**, *42*, 222−230.

(4) Winkler, J. R.; Gray, H. B. Electronic Structure of Metal-oxo Ions. *Struct. Bonding (Berlin, Ger.)* **2011**, *142*, 17−28.

(5) Holm, R. H. Metal-centered Oxygen Atom Transfer Reactions. *Chem. Rev.* **1987**, *87*, 1401−1449.

(6) Zhang, B.; Hemann, C. F.; Hille, R. Kinetic and Spectroscopic Studies of the Molybdenum-Copper CO Dehydrogenase from Oligotrophacarboxidovorans. *J. Biol. Chem.* **2010**, *285*, 12571−12578.

(7) Shanmugam, M.; Wilcoxen, J.; Habel-Rodriguez, D.; Cutsail, G. E.; Kirk, M. L.; Hoffman, B. M.; Hille, R. ^{13}C and 63,65 Cu ENDOR Studies of CO Dehydrogenase from OligotrophaCarboxidovorans. Experimental Evidence in Support of a Copper−Carbonyl Intermediate. *J. Am. Chem. Soc.* **2013**, *135*, 17775−17782.

(8) Breglia, R.; Bruschi, M.; Cosentino, U.; De Gioia, L.; Greco, C.; Miyake, T.; Moro, G. A theoretical study on the reactivity of the Mo/Cu-containing carbon monoxide dehydrogenase with dihydrogen. *Protein Eng., Des. Sel.* **2016**, *30*, 169−174.

(9) Stein, B. W.; Kirk, M. L. Orbital Contributions to CO Oxidation in Mo−Cu Carbon Monoxide Dehydrogenase. *Chem. Commun.* **2014**, *50*, 1104−1106.

(10) Rovaletti, A.; Bruschi, M.; Moro, G.; Cosentino, U.; Greco, C. The Challenging in silico Description of Carbon Monoxide Oxidation as Catalyzed by Molybdenum-Copper CO Dehydrogenase. *Front. Chem.* **2019**, *6*, 630.

(11) Xu, K.; Hirao, H. Revisiting the Catalytic Mechanism of Mo−Cu Carbon Monoxide Dehydrogenase Using QM/MM and DFT Calculations Phys. *Phys. Chem. Chem. Phys.* **2018**, *20*, 18938−18948.

(12) Hofmann, M.; Kassube, J. K.; Graf, T. The Mechanism of Mo-/Cu-dependent CO Dehydrogenase. *JBIC, J. Biol. Inorg. Chem.* **2005**, *10*, 490−495.

(13) Rokhsana, D.; Large, T. A. G.; Dienst, M. C.; Retegan, M.; Neese, F. A Realistic in silico Model for Structure/Function Studies of Molybdenum-Copper CO Dehydrogenase. *JBIC, J. Biol. Inorg. Chem.* **2016**, *21*, 491−499.

(14) Siegbahn, P. E. M.; Shestakov, A. F. Quantum Chemical Modeling of CO Oxidation by the Active Site of Molybdenum CO Dehydrogenase. *J. Comput. Chem.* **2005**, *26*, 888−898.

(15) Majumdar, A. Bioinorganic Modeling Chemistry of Carbon Monoxide Dehydrogenases: Description of Model Complexes, Current Status and Possible Future Scopes. *Dalton Trans* **2014**, *43*, 12135−12145.

(16) Gourlay, C.; Nielsen, D. J.; White, J. M.; Knottenbelt, S. Z.; Kirk, M. L.; Young, C. G. Paramagnetic Active Site Models for the Molybdenum-Copper Carbon Monoxide Dehydrogenase. *J. Am. Chem. Soc.* **2006**, *128*, 2164−2165.

(17) Gourlay, C.; Nielsen, D. J.; Evans, D. J.; White, J. M.; Young, C. G. Models for Aerobic Carbon Monoxide Dehydrogenase. *Chem. Sci.* **2018**, *9*, 876−888.

(18) Takuma, M.; Ohki, Y.; Tatsumi, K. Sulfido-bridged DinuclearMolybdenum-Copper Complexes Related to the Active Site of CO Dehydrogenase: $[(\text{dithiolate})\text{Mo}(\text{O})\text{S}_2\text{Cu}(\text{SAr})]^{2-}$ (Dithiolate = = $1,2\text{-S}_2\text{C}_6\text{H}_4$, $1,2\text{-S}_2\text{C}_6\text{H}_2\text{-3,6-Cl}_2$, $1,2\text{-S}_2\text{C}_2\text{H}_4$). *Inorg. Chem.* **2005**, *44*, 6034−6043.

(19) Enemark, J. H.; Cooney, J. J. A.; Wang, J.-J.; Holm, R. H. Synthetic Analogues and Reaction Systems Relevant to the Molybdenum and Tungsten Oxotransferases. *Chem. Rev.* **2004**, *104*, 1175−1200.

(20) Holm, R. H.; Solomon, E. I.; Majumdar, A.; Tenderholt, A. Comparative Molecular Chemistry of Molybdenum and Tungsten and Its Relation to Hydroxylase and Oxotransferase Enzymes. *Coord. Chem. Rev.* **2011**, *255*, 993−1015.

(21) Groysman, S.; Majumdar, A.; Zheng, S.-L.; Holm, R. H. Reactions of MonodithioleneTungsten(VI) Sulfido Complexes with Copper(I) in Relation to the Structure of the Active Site of Carbon Monoxide Dehydrogenase. *Inorg. Chem.* **2010**, *49*, 1082−1089.

(22) Groysman, S.; Wang, J.-J.; Tagore, R.; Lee, S. C.; Holm, R. H. A Biomimetic Approach to Oxidized Sites in the Xanthine Oxidoreductase Family: Synthesis and Stereochemistry of Tungsten(VI) Analogue Complexes. *J. Am. Chem. Soc.* **2008**, *130*, 12794−12807.

(23) Wang, J.-J.; Groysman, S.; Lee, S. C.; Holm, R. H. Synthesis of Structural Analogues of the Oxidized Sites in the Xanthine Oxidoreductase Enzyme Family. *J. Am. Chem. Soc.* **2007**, *129*, 7512−7513.

(24) Groysman, S.; Holm, R. H. A Series of Mononuclear Quasi-Two-Coordinate Copper(I) Complexes Employing a Sterically Demanding Thiolate Ligand. *Inorg. Chem.* **2009**, *48*, 621−627.

(25) Ferrara, S. J.; Wang, B.; Haas, E.; LeBlanc, K. W.; Mague, J. T.; Donahue, J. P. Synthesis and Structures of $[\text{LCu(I)}(SSi^{iii}\text{Pr}_3)]$ (L = = triphos, carbene) and Related Compounds. *Inorg. Chem.* **2016**, *55* (18), 9173−9177.

(26) Mouchfiq, A.; Todorova, T. K.; Dey, S.; Fontecave, M.; Mougel, V. A Bioinspired Molybdenum−Copper Molecular Catalyst for CO_2Electroreduction. *Chem. Sci.* **2020**, *11*, 5503−5510.

(27) Ghosh, D.; Sinhababu, S.; Santarsiero, B. D.; Mankad, N. P. A W/Cu Synthetic Model for the Mo/Cu Cofactor of Aerobic CODH indicates that Biochemical CO Oxidation Requires a Frustrated Lewis Acid/Base Pair. *J. Am. Chem. Soc.* **2020**, *142*, 12635−12642.

(28) Hollingsworth, T. S.; Hollingsworth, R. L.; Lord, R. L.; Groysman, S. Cooperative Bimetallic Reactivity of a Heterodinuclear Molybdenum-Copper Model of Mo-Cu CODH. *Dalton Trans* **2018**, *47*, 10017−10024.

(29) Chang, C. J.; Deng, Y.; Shi, C.; Chang, C. K.; Anson, F. C.; Nocera, D. G. Electrocatalytic Four-electron Reduction of Oxygen to Water by a Highly Flexible Cofacial Cobalt Bisporphyrin. *Chem. Commun.* **2000**, 1355−1356.

(30) Chang, C. J.; Loh, Z.-H.; Shi, C.; Anson, F. C.; Nocera, D. G. Targeted Proton Delivery in the Catalyzed Reduction of Oxygen to Water by Bimetallic Pacman Porphyrins. *J. Am. Chem. Soc.* **2004**, *126*, 10013−10020.
(31) Haack, P.; Limberg, C.; Tietz, T.; Metzinger, R. Unprecedented Binding and Activation of CS2 in a Dinuclear Copper(I) Complex. *Chem. Commun.* **2011**, *47*, 6374−6376.
(32) Pilz, M. F.; Limberg, C.; Lazarov, B. B.; Hultzsch, K. C.; Ziemer, B. Dinuclear Zinc Complexes Based on Parallel β-Diiminato Binding Sites: Syntheses, Structures, and Properties as CO2/Epoxide Copolymerization Catalysts. *Organometallics* **2007**, *26*, 3668−3676.
(33) Chen, Z.; Zhao, X.; Gong, X.; Xu, D.; Ma, Y. Macrocyclic Trinuclear Nickel Phenoxyimine Catalysts for High-Temperature Polymerization of Ethylene and Isospecific Polymerization of Propylene. *Macromolecules* **2017**, *50*, 6561−6568.
(34) Han, S.; Yao, E.; Qin, W.; Zhang, S.; Ma, Y. Binuclear Heteroligated Titanium Catalyst Based on Phenoxyimine Ligands: Synthesis, Characterization, and Ethylene (Co)polymerization. *Macromolecules* **2012**, *45*, 4054−4059.
(35) Takeuchi, D.; Chiba, Y.; Takano, S.; Osakada, K. Double-Decker-Type Dinuclear Nickel Catalyst for Olefin Polymerization: Efficient Incorporation of Functional Co-monomers. *Angew. Chem., Int. Ed.* **2013**, *52*, 12536−12540.
(36) Takano, S.; Takeuchi, D.; Osakada, K. Olefin Polymerization Catalyzed by Double-Decker Dipalladium Complexes: Low Branched Poly(α-Olefin)s by Selective Insertion of the Monomer Molecule. *Chem. - Eur. J.* **2015**, *21*, 16209−16218.
(37) Hollingsworth, R. L.; Bheemaraju, A.; Lenca, N.; Lord, R. L.; Groysman, S. Divergent Reactivity of a New Dinuclear Xanthene-bridged Bis(iminopyridine) Di-nickel Complex with Alkynes. *Dalton Trans.* **2017**, *46*, 5605−5616.
(38) Hollingsworth, R. L.; Beattie, J. W.; Grass, A.; Groysman, S.; Martin, P. D.; Lord, R. L. Reactions of DicobaltOctacarbonyl with Dinucleating and MononucleatingBis(imino)pyridine Ligands. *Dalton Trans* **2018**, *47*, 15353−15363.
(39) Rong, C.; Wang, F.; Li, W.; Chen, M. Ethylene Polymerization by Dinuclear Xanthene-Bridged Imino- and Aminopyridyl Nickel Complexes. *Organometallics* **2017**, *36*, 4458−4464.
(40) Hirotsu, M.; Ohno, N.; Nakajima, T.; Kushibe, C.; Ueno, K.; Kinoshita, I. Synthesis and Characterization of Xanthene-bridged Schiff-baseDimanganese(III) Complexes: Bimetallic Catalysts for Asymmetric Oxidation of Sulfides. *Dalton Trans* **2010**, *39*, 139−148.
(41) Wang, R.; Sui, X.; Pang, W.; Chen, C. Ethylene Polymerization by Xanthene-Bridged Dinuclearα-DiimineNi^{II} Complexes. *ChemCatChem* **2016**, *8*, 434−440.
(42) Gatus, M. R. D.; Bhadbhade, M.; Messerle, B. A. Highly Versatile Heteroditopic Ligand Scaffolds for Accommodating Group 8, 9 & 11 Heterobimetallic Complexes. *Dalton Trans* **2017**, *46*, 14406−14419.
(43) Haas, R. M.; Arshad, M.; Anthony, J. A.; Altmann, P. J.; Pöthig, A.; Köhler, F. H.; Hess, C. R. Six- and Seven-coordinate Fe(II) and Zn(II) Compounds Ligated by Unsymmetric Xanthene-based Ligands: Characterization and Magnetic properties. *Inorg. Chem. Front.* **2016**, *3*, 616−629.
(44) Do, T. H.; Brown, S. N. Mono- and Bimetallic Pentacoordinate Silicon Complexes of a Chelating Bis(catecholimine) Ligand. *Dalton Trans* **2019**, *48*, 11565−11574.
(45) Do, T. H.; Brown, S. N. Synthesis, Dynamics and Redox Properties of Eight-coordinate Zirconium Catecholate Complexes. *Dalton Trans* **2020**, *49*, 11648−11656.
(46) Dziembowska, T.; Rozwadowski, Z.; Filarowski, A.; Hansen, P. E. NMR Study of Proton Transfer Equilibrium in Schiff Bases Derived from 2-hydroxy-1-naphthaldehyde and 1-hydroxy-2-acetonaphthone. Deuterium Isotope Effects on ^{13}C and ^{15}N Chemical Shifts. *Magn. Reson. Chem.* **2001**, *39*, S67−S80.
(47) Shannon, R. D. Revised Effective Ionic Radii and Systematic Studies of Interatomic Distances in Halides and Chalcogenides. *Acta Crystallogr., Sect. A: Cryst. Phys., Diffr., Theor. Gen. Crystallogr.* **1976**, *A32*, 751−767.
(48) Monteiro, B.; Cunha-Silva, L.; Gago, S.; Klinowski, J.; Paz, F. A. A.; Rocha, J.; Goncalves, I. S.; Pillinger, M. Crystal and supramolecular structures of dioxomolybdenum(VI) and dioxotungsten(VI) complexes of dihydroxybenzoic acids. *Polyhedron* **2010**, *29*, 719−730.
(49) Litos, C.; Karaliota, A.; Parsons, S. Bis(tetra-phenyl-phosphonium) bis−(1-carb-oxy-benzene-2,3-diolato-κ2O,O′)-cis-dioxomolybdate(VI). *Acta Crystallogr., Sect. E: Struct. Rep. Online* **2006**, *62*, No. m928.
(50) Amiri Rudbari, H.; Khorshidifard, M.; Askari, B.; Habibi, N.; Bruno, G. New asymmetric Schiff base ligand derived from allylamine and 2,3-dihydroxybenzaldehyde and its molybdenum(VI) complex: Synthesis, characterization, crystal structures, computational studies and antibacterial activity together with synergistic effect against Pseudomonas aeroginosa PTTC 1570. *Polyhedron* **2015**, *100*, 180−191.

https://doi.org/10.1021/acs.inorgchem.1c01735
Inorg. Chem. 2021, 60, 14655−14666